A Comparative Study of Copper Chalcogenide Nanocrystals as Agents for Photothermal Therapy

Soohyung Lee

A thesis

submitted in partial fulfillment of the

requirements for the degree of

Master of Science in Chemical Engineering

University of Washington

2016

Reading Committee:

Vincent C. Holmberg, Chair

Qiuming Yu

Program Authorized to Offer Degree:

Chemical Engineering

University of Washington

Abstract

A Comparative Study of Copper Chalcogenide Nanocrystals as Agents for Photothermal Therapy

Soohyung Lee

Chair of the Supervisory Committee:
Assistant Professor Vincent C. Holmberg
Department of Chemical Engineering

In recent years, copper sulfide nanocrystals (NCs) have emerged as promising candidates for new photothermal agents due to their strong near-infrared (NIR) light absorption, high photostability, low toxicity, and suitable size for photothermal therapy.[1,2] However, the low photothermal conversion efficiency of copper sulfide NCs in the tissue transparency window from 650 to 900 nm hinders further development of copper sulfide as an effective photothermal agent.[3,4] Therefore, it is still necessary to improve the photothermal conversion efficiency near 800 nm for these materials to be used effectively in photothermal therapy.[4]

As a result, other kinds of copper chalcogenide NCs, such as copper selenide, copper telluride, and their alloys have been recently proposed.[5,6,7] By changing the mix of chalcogen

substituents in the NC, the localized surface plasmon resonance (LSPR) position can be tuned to more closely match the tissue transparency window, leading to a higher photothermal conversion efficiency near the excitation wavelength.[8] Copper selenide-sulfide and copper telluride-sulfide alloy NCs are especially interesting candidate materials for photothermal agents, as they should have lower cytotoxicity than pure copper selenide and copper telluride NCs due to their reduced selenium and tellurium content. However, their potential use for photothermal therapy has not yet been evaluated in depth.

Herein, the photothermal conversion efficiency of several copper chalcogenide alloy NCs were investigated to evaluate the potential use of each as a photothermal agent via a comparison with unalloyed copper sulfide NCs. By controlling the composition of the alloys, their localized surface plasmon resonance peaks could be tuned throughout the near-infrared region, potentially leading to materials with resonances more closely matched to ideal therapeutic windows. Moreover, it was found that the photothermal conversion efficiency increased relative to the copper sulfide NCs as the LSPR peaks were tuned more closely to the 808 nm laser wavelength used in this study – directly within the center of the tissue transparency window.

TABLE OF CONTENTS

LIST OF FIGURES

LIST OF TABLES

ACKNOWLEDGEMENTS

First and foremost, I would like to thank my advisor, Dr. Vincent Holmberg, for his support, encouragement, and guidance during my thesis. His door was always open for discussions to develop my project. Without his guidance, this work would not have been possible.

Also, I am extremely grateful to my group members, Elena Pandres, Grant Williamson, Brittany Bishop, Binh Dang, Reyn Aoki, and Fahad Alamer for giving me invaluable ideas and suggestions throughout my work. I also would like to thank Prof. Qiuming Yu for being a part of my thesis committee and reviewing my research work.

I also appreciate the help and friendship of the Pozzo group members, David Li and Yi-Ting Lee, that helped set up the photothermal conversion measurements. Also, I gratefully thank all my friends and colleagues who supported me and encouraged me to finish my thesis.

Last but not least, I would like to express my deepest thanks to my family for their unconditional love and support. Especially, I am sincerely thankful to my parents for their support throughout my entire life.

Chapter 1. INTRODUCTION

1.1 LOCALIZED SURFACE PLASMON RESONANCES (LSPRS)

Localized surface plasmon resonances (LSPRs) are collective oscillations of free charge carriers, in resonance with specific wavelengths of incident light, that produce intense electromagnetic fields at the surface of nanostructures. These collective charge density oscillations result in strong absorption and scattering of light at a particular resonant frequency that depends on the surrounding dielectric environment, as well as size, shape, composition and electronic characterstics of the nanostructures.[9,10,11]

LSPRs are commonly observed in noble metal nanostructures due to the resonant interaction of their free electrons with the electromagnetic field of impinging light.[12] However, LSPRs are not exclusively limited to metal nanocrystals and also can be observed in nonmetallic nanomaterials that possess appreciable free carrier concentrations.[9,12,13] Recently, many studies have explored the plasmonic properties of several types of semiconductor nanocrystals, including the copper chalcogenides[13,14,15], tin-doped indium oxide[16], aluminum-doped zinc oxide[17], and phosphorus-doped silicon NCs.[18]

Semiconductor nanostructures have emerged as a new family of plasmonic materials with highly tunable plasmonic properties that can be engineered compositionally by including designated impurities that are incorporated in different quantities and at different energy levels.[9,12,13] This is due to the fact that their LSPR frequency can be tuned greatly through changes in the density of free charge carriers which are controlled by the degree of doping, unlike metallic nanostructures which have nearly fixed charge carrier density.[9,12,13] Although it is known that the LSPR characteristics of noble metal nanoparticles can be tuned by variation of

the size, shape, choice of metal, or dielectric environment of the nanoparticles, metallic nanostructures lack wide-range compositional tunability.[19] As a result, plasmonic semiconductor nanocrystals are an attractive subset of materials that can be engineered compositionally in a variety of research applications that utilize plasmonic effects.

1.2. Plasmonic Nanomaterials for Photothermal Therapy

Plasmonic nanomaterials have received considerable attention for both their fundamental properties and potential applications – from therapy and medical diagnostics to optoelectronics – due to their unique interaction with light via plasmon resonance.[11,20] One of the major applications of plasmonic NCs is photothermal therapy. Photothermal therapy (PTT) is a minimally-invasive cancer treatment that uses local hyperthermia to kill cancerous cells, which can be highly sensitive to large temperature increases.[20,21]

Effective thermal ablation of cancer cells can be induced by laser irradiation combined with targeted plasmonic nanostructures that act as photothermal agents that convert absorbed photon energy to thermal energy to increase temperature locally and kill the cancerous cells.[20,22] There is an especially increasing interest in PTT using near-infrared (NIR) lasers as an alternative way to destroy tumor tissue, as opposed to invasive conventional approaches. NIR radiation is used to allow the laser to penetrate deeply into biological tissues with high intensity due to the low attenuation of light by hemoglobin and water in the NIR window (from 650 to 900 nm).[5,22,23,24,25]

Among the many plasmonic nanostructures that exist, gold nanostructures of various geometries have been studied widely for photothermal therapy (PTT) over the past decades. This is due to the fact that the LSPR characteristics of gold nanostructures can be tuned throughout the NIR by modifying their size, shape, and structure.[20] For example, gold nanoshells, nanorods,

and nanocages have all been evaluated and used as photothermal agents that absorb NIR light;[20,26,27,28] however, several limitations – such as low photostability, costly and complicated synthesis, and non-degradability – lead to the need for better photothermal agents.[1,29]

1.3. Copper Chalcogenide Nanocrystals as Photothermal Agents

Recently, copper sulfide NCs have been explored as alternative photothermal agents due to several advantages over conventional gold nanostructures.[1] First, in order to tune the gold LSPR band into the NIR region, it is necessary to form large, anisotropic gold nanostructures or hard-to-synthesize gold nanoshells. In contrast, copper sulfide NCs are capable of absorbing NIR light through the resonant excitation of high concentrations of free charge carriers (in this case hole carriers generated by vacancy-doping), which leads to an intrinsic plasmon band in the NIR while maintaining a small, spherical geometry – thus potentially increasing bloodstream circulation time.[1,5] Second, the robust photostability of copper sulfide NCs under NIR laser irradiation makes them potential candidates for use as effective photothermal agents under long periods of laser irradiation.[2,30] Finally, copper sulfide NCs exhibit relatively low toxicity, showing promise for safe photothermal applications.[1,31] Importantly, due to their small size, copper sulfide NCs less than 6 nm in diameter can easily be cleared from the body by the renal system.[1]

Nonetheless, copper sulfide still has limited photothermal conversion efficiency when driven by 808 nm irradiation, which is one of the commonly used laser wavelengths for photothermal therapy due to the low level of heat generation from water at this wavelength.[5,22,25,31] Thus, copper selenide[5], copper telluride[6], and their alloy NCs[7] have been recently proposed as alternative agents for photothermal therapy. This is due to the fact that their

LSPR peaks are more closely matched to the laser wavelength, so that they could potentially achieve higher photothermal conversion efficiencies.[8] Copper selenide-sulfide and copper telluride-sulfide alloy NCs are especially exciting candidate materials that are worth testing as photothermal agents, as these materials potentially have lower cytotoxicity than pure copper selenide and copper telluride NCs due to their reduced selenium and tellurium content.

Chapter 2. EXPERIMENTAL METHODS

2.1. MATERIALS AND REAGENTS

Copper(I) chloride (CuCl, 99.995%), sulfur powder (S, 99.998%), selenium powder (Se, 99.99%), tellurium powder (Te, 99.997%), 1-dodecanethiol (DDT, ≥98%), oleylamine (OAM, ≥98%), oleic acid (OA, 90%), toluene (anhydrous, 99.8%), and chloroform (anhydrous, ≥99%) were purchased from Sigma-Aldrich. Copper(II) acetylacetonate ($Cu(acac)_2$, 98%), and ethanol (anhydrous, 200 proof, ≥99.5%) were obtained from Acros Organics. Ultrapure trace metal grade hydrochloric acid (HCl, 34-37%), and ultrapure trace metal grade nitric acid (HNO_3, 67-70%) were supplied by Fisher Scientific. Methoxy polyethylene glycol thiol (mPEG-SH, 10 kDa) was bought from Creative PEGWorks. All chemicals were used without further purification.

2.2. NANOCRYSTAL SYNTHESES

A glove box (H_2O < 0.5 ppm, O_2 < 0.5 ppm) was used to store and handle all air- and moisture-sensitive chemicals. All syntheses were carried out under nitrogen atmosphere using standard Schlenk line techniques.

2.2.1 *Synthesis of $Cu_{2-x}S$ Nanocrystals*

The synthesis of $Cu_{2-x}S$ NCs was performed according to procedures developed by Saldanha *et al*.[7] In a typical synthesis, 0.8 mmol of copper(II) acetylacetonate (210 mg) and 0.4 mmol of sulfur (12.8 mg) were combined with 4 mL of 1-dodecanethiol and 8 mL of oleic acid in a three neck round bottom flask. The mixture was heated to 80°C and degassed under vacuum for 1 hr with vigorous stirring. Afterwards, the temperature was raised to 220°C under nitrogen atmosphere, and the mixture was allowed to react at this temperature for 30 min. After 30 min, the flask was rapidly cooled to room temperature by using a water bath. Once at room temperature, 15mL of ethanol was added to the reaction solution, followed by centrifuging at 8000 rpm (7,452 x g) for 20 min. The supernatant was discarded and the precipitate was dispersed in 5 mL of toluene. The washing procedure was repeated one more time to clean the sample effectively. Finally, the nanocrystals were dispersed in 5 mL of clean toluene and centrifuged at 1500 rpm (262 x g) for 1 min to remove aggregated and poorly-capped nanocrystals.

2.2.2. *Synthesis of $Cu_{2-x}Se_yS_{1-y}$ Nanocrystals*

The synthesis of copper selenide-sulfide NCs was carried out using the method of Liu *et al*.[32] First, oleic acid-selenium and oleylamine-sulfur complexes were prepared in a molar ratio of 2:1 OA-Se to OAm-S. In detail, OAm-S was prepared by mixing 2 mmol of S powder (64 mg) with 10 mL of OAm at 110°C for 30 min under nitrogen atmosphere. For preparation of the OA-Se precursor, 2 mmol of Se powder (160 mg) was dissolved in 10 mL of OA at 330°C under nitrogen. The solution was held at this temperature for 2 hrs, and then cooled to 80°C for further use.

Meanwhile, for the synthesis of copper selenide-sulfide nanocrystals, 1 mmol of copper(I) chloride (0.198 g) was mixed with 10 mL of oleylamine in a three neck round bottom flask under vigorous stirring. The solution was heated to 80°C and degassed for 30 min. Then, the temperature was increased to 225°C in order to form an organometallic oleylamine-copper precursor complex. Meanwhile, the OA-Se and OAm-S precursors were mixed in a 2:1 molar ratio. As soon as the chalcogen precursor mixture was prepared, 5mL of the OA-Se/OAm-S precursor solution was injected into the copper precursor solution at 225°C. The reaction temperature decreased to 200°C after the injection. The reaction proceeded at this temperature for 2.5 min, and then the flask was removed from the heating mantle to decrease the temperature to 60°C. In order to prevent solidification, 5 mL of toluene were added into the solution at 60°C. The nanocrystals were washed by the addition of 10 mL of ethanol, followed by centrifugation at 8000 rpm (7,452 x g) for 3 min. The supernatant was discarded and the precipitate was dispersed in 5 mL of chloroform. The purification was repeated twice to clean the sample thoroughly. Finally, the nanocrystals were dispersed in 5 mL of clean chloroform.

2.2.3. *Synthesis of $Cu_{2-x}Te_yS_{1-y}$ Nanocrystals*

Copper telluride-sulfide NCs were synthesized via a modified version of a procedure introduced by Saldanha *et al*.[7] To synthesize $Cu_{2-x}Te_yS_{1-y}$ NCs, 1.2 mmol of copper(II) acetylacetonate (315 mg) and 0.6 mmol of tellurium (78 mg) were mixed with 6 mL of 1-dodecanethiol in a three neck round bottom flask. The mixture was degassed overnight at 80°C with vigorous stirring. Then, the flask was heated to 240°C under nitrogen atmosphere. After the reaction temperature reached 240°C, the heating mantle was immediately removed and cooled to room temperature by using a water bath. The nanocrystals were precipitated by centrifugation at 8000 rpm (7,452 x g) for 10 min with the addition of 5 mL of ethanol. The cleaning procedure

was repeated one more time to remove unreacted precursors and byproducts. Finally, the nanocrystals were dispersed in 5 mL of toluene and centrifuged at 1500 rpm (262 x g) for 1 min to remove poorly stabilized nanocrystals.

2.2.4. *Ligand Exchange*

To make the initially hydrophobic nanocrystals dispersible in water, methoxy-polyethylene glycol thiol (mPEG-SH, 10 kDa) was used for ligand exchange according to the method described by Chen *et al*.[33] Briefly, 200 µL of the nanocrystal dispersion (in chloroform) containing approximately 1.5 mg of nanocrystals was mixed in a vial with 200 µL of a freshly prepared chloroform solution containing 30 mg of mPEG-SH, followed by the addition of 20 µL of 15 nM $NaBH_4$ in methanol as a reducing agent. The mixture was stirred gently for 1 day at room temperature. Then, the ligand-exchanged NCs were precipitated by adding 2 mL of hexanes followed by centrifugation at 8000 rpm (7,452 x g) for 5 min. The supernatant was discarded, and the precipitated NCs were dispersed in 200 µL of methanol. Finally, the methanol was evaporated under vacuum using a rotary evaporator, and the mPEG-SH functionalized nanocrystals were dispersed in 3 mL of (18.2 MΩ) deionized water.

2.3. Characterization Methods

2.3.1. *Transmission Electron Microscopy (TEM)*

TEM samples were prepared by dropping 15 µL of dilute nanocrystal dispersion in organic solvents or deionized water on carbon-coated 200 mesh nickel TEM grids (Electron Microscopy Sciences) sitting on filter paper. Samples were imaged using a FEI Tecnai G2 F20 transmission electron microscope operated at an accelerating voltage of 200 kV.

2.3.2. *Energy Dispersive X-ray Spectroscopy (EDS)*

Energy-dispersive X-ray spectroscopy (EDS) was carried out using a transmission electron microscope (FEI Tecnai G2 F20) equipped with an X-ray energy-dispersive spectroscopy detector (EDAX Element Silicon Drift Detector) in order to analyze the composition of nanocrystals dispersed onto a carbon-coated 200 mesh nickel TEM grid.

2.3.3. *X-ray Diffraction (XRD)*

Samples were prepared by drop casting concentrated NC dispersions onto a silicon substrate. XRD patterns were recorded using a Bruker D8 diffractometer with a Cu Kα X-ray source at 45 kV and 120 mA. Scans were performed from 19 - 88° in 0.02 (2θ°) increments for 2 hours.

2.3.4. *UV-vis-NIR Spectroscopy*

Extinction spectra of all NC dispersions were measured in a 1 cm path length quartz cuvette (Spectrocell) using Varian Cary 60 UV-vis and Varian Cary 5000 UV-vis-NIR spectrophotometers. All measurements were carried out at optical densities ≤ 1.0.

2.3.5. *Inductively Coupled Plasma Atomic Emission Spectroscopy (ICP-AES)*

To determine the concentration of each sample, inductively coupled plasma atomic emission spectroscopy (ICP-AES) analysis was performed using a Perkin Elmer Optima 8300. Nanocrystals were digested in aqua regia prepared from ultrapure nitric acid and hydrochloric acid in a 1:3 volume ratio. Once digestion was complete, samples were diluted using (18.2 MΩ) deionized water. Calibrations were performed using multi-element VII and sulfur ICP-AES standards obtained from EMD Millipore and Sigma-Aldrich, respectively. 327.393 nm, 181.975

nm, 196.026 nm, and 214.281 nm spectral lines were used to determine the copper, sulfur, selenide, and telluride concentration in each sample, respectively.

Chapter 3. RESULTS AND DISCUSSION

3.1. Synthesis of Copper Chalcogenide Nanocrystals

In order to study the photothermal conversion efficiency of copper chalcogenide nanocrystals with different compositions and LSPR peak positions, copper chalcogenide nanocrystals of similar size but varied composition were synthesized. Efforts were taken to minimize differences in average size between samples due to the fact that photothermal conversion efficiency is correlated with the ratio of the absorption to extinction that is affected by the size of nanocrystals.[34]

Figure 3.1 shows representative TEM images of the copper chalcogenide nanocrystals obtained by the procedures described above.

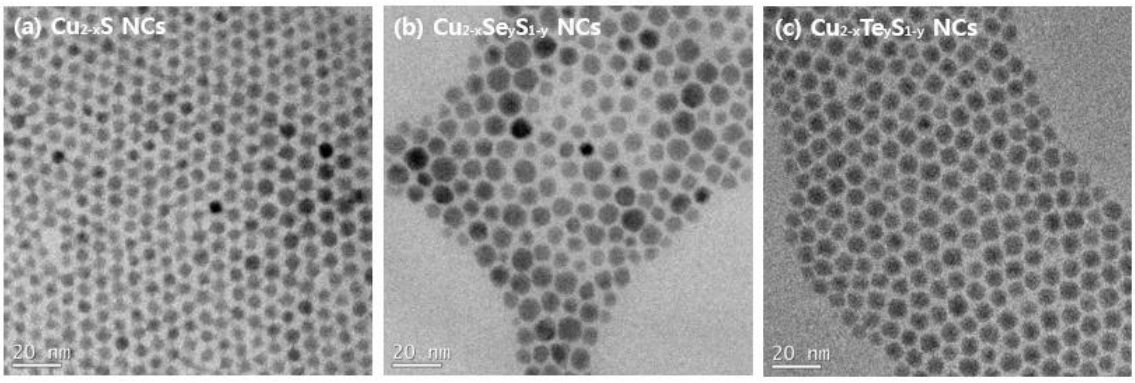

Figure 3.1. TEM images of (a) $Cu_{2-x}S$, (b) $Cu_{2-x}Se_yS_{1-y}$, and (c) $Cu_{2-x}Te_yS_{1-y}$ NCs with average diameters of 5.2 ± 0.3, 6.5 ± 0.7, and 6.2 ± 0.3 nm, respectively.

TEM analysis shows that $Cu_{2-x}S$, $Cu_{2-x}Se_yS_{1-y}$, and $Cu_{2-x}Te_yS_{1-y}$ NCs are roughly spherical in shape with average diameters of 5.2 ± 0.3, 6.5 ± 0.7, and 6.2 ± 0.3 nm, respectively. Their corresponding size distributions are shown in Appendix A in Figure A.1.

In addition, the chemical composition of the nanocrystals was determined by energy dispersive X-ray spectroscopy (EDS). The measured copper chalcogenide atomic ratios and weight ratios are listed in Table 3.1. The corresponding EDS data are reported in Appendix A in Figure A.2.

Table 3.1. Elemental compositions of $Cu_{2-x}S$, $Cu_{2-x}Se_yS_{1-y}$, and $Cu_{2-x}Te_yS_{1-y}$ NCs

	Atomic (%)			Weight (%)		
$Cu_{2-x}S$	**Cu**		**S**	**Cu**		**S**
	64.8		35.2	78.5		21.5
$Cu_{2-x}Se_yS_{1-y}$	**Cu**	**Se**	**S**	**Cu**	**Se**	**S**
	63.7	18.0	18.3	66.8	23.5	9.7
$Cu_{2-x}Te_yS_{1-y}$	**Cu**	**Te**	**S**	**Cu**	**Te**	**S**
	62.2	18.6	19.2	57.0	34.1	8.9

EDS analysis revealed that the copper sulfide, selenide-sulfide, and telluride-sulfide NCs have the following stoichiometries: $Cu_{1.84}S$, $Cu_{1.75}Se_{0.50}S_{0.50}$, and $Cu_{1.65}Te_{0.49}S_{0.51}$, respectively. The results indicate that the copper chalcogenide alloy NCs support higher copper vacancy concentrations than the pure copper sulfide NCs.[35] Furthermore, the above elemental compositions for copper selenide-sulfide and telluride-sulfide ternary alloyed NCs provide evidence for the incorporation of Se and Te in the final products.

For all samples, XRD analysis was carried out in an attempt to determine the crystal structure of the copper chalcogenide nanocrystals, and provide evidence for the formation of copper chalcogenide alloy nanocrystals.

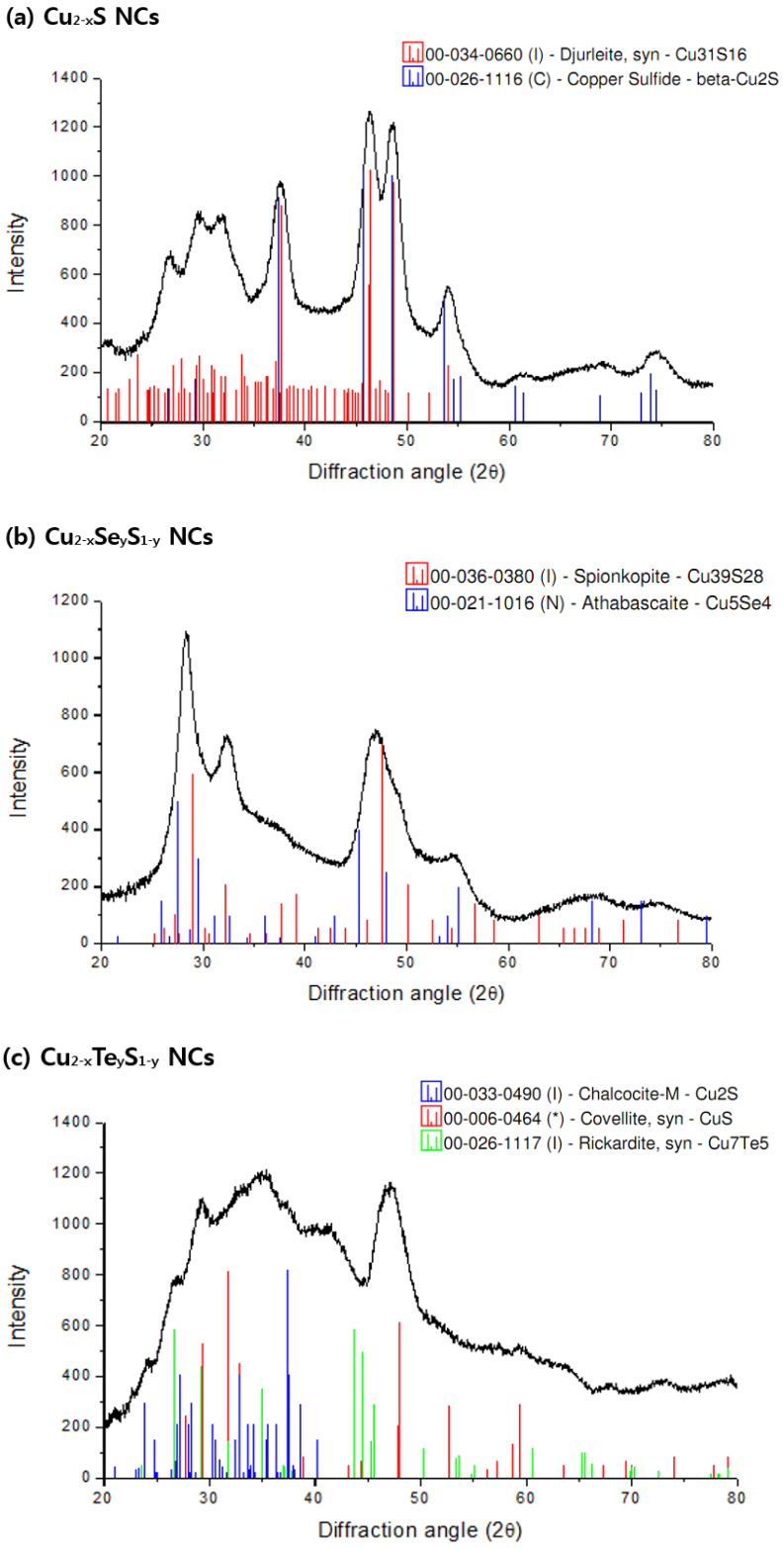

Figure 3.2. XRD patterns of (a) $Cu_{2-x}S$, (b) $Cu_{2-x}Se_yS_{1-y}$, and (c) $Cu_{2-x}Te_yS_{1-y}$ NCs.

Figure 3.2 presents the XRD patterns of $Cu_{2-x}S$, $Cu_{2-x}Se_yS_{1-y}$, and $Cu_{2-x}Te_yS_{1-y}$ NCs. It is especially difficult to determine copper chalcogenide crystal structures, as they have a diverse composition and numerous crystallographic phases. Even a slight change in the reaction temperature is able to cause the formation of a different crystal structure, or even mixed phases within a single batch.[7,36] Even though XRD analysis for copper chalcogenide NCs is challenging, XRD patterns for the samples obtained were closely matched with the reference lines shown in the Figure 3.2. For example, the XRD peaks of the $Cu_{2-x}S$ nanocrystals correspond well with the djurleite ($Cu_{31}S_{16}$; PDF card 00-034-0660) and β copper sulfide (Cu_2S, 00-026-1116) phases. Moreover, the diffraction peaks of the copper chalcogenide ternary alloyed NCs shift to smaller Bragg angles, as compared to the copper sulfide references, corroborating alloy formation. This is due to the fact that the increase in the lattice constant by the partial substitution of larger selenium and tellurium anions with sulfur anions leads to a decrease in Bragg angle.[7,32]

3.2. Localized Surface Plasmon Characteristics of Copper Chalcogenide Nanocrystals

As can be seen in Figure 3.3, UV-vis-NIR spectroscopy shows the tunable LSPR response of the copper chalcogenide NCs that arises from the appreciable concentration of holes in the valence band, which are generated by the large number of copper vacancies present in the material.[9,12,13]

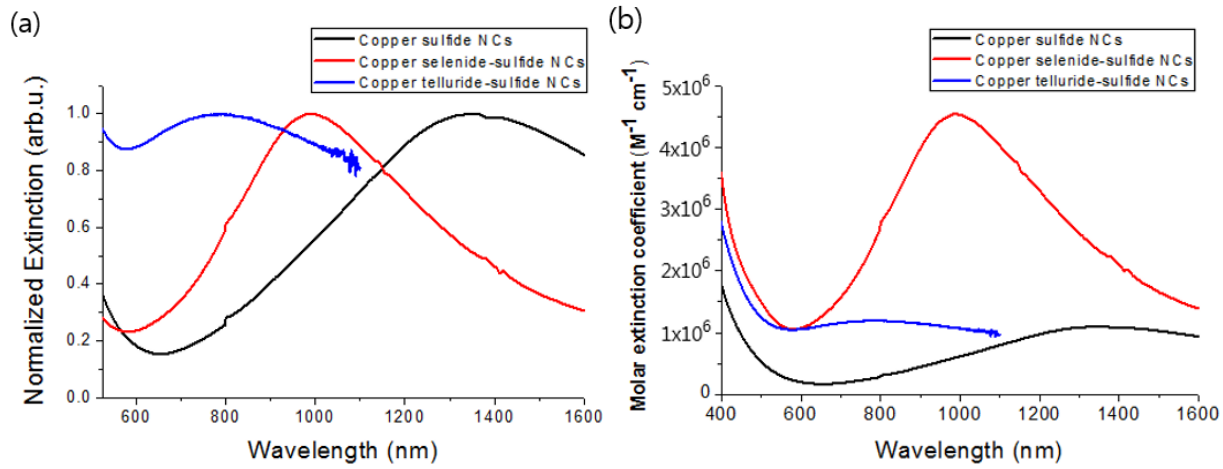

Figure 3.3. (a) The normalized extinction spectra of $Cu_{2-x}S$, $Cu_{2-x}Se_yS_{1-y}$, and $Cu_{2-x}Te_yS_{1-y}$ NCs in toluene. (b) The calculated molar extinction coefficient of $Cu_{2-x}S$, $Cu_{2-x}Se_yS_{1-y}$, and $Cu_{2-x}Te_yS_{1-y}$ NCs (in terms of moles of nanocrystals per volume of solvent) based on the absorbance spectrum of samples dispersed in toluene with Cu concentrations of 100 ppm, as determined by ICP-AES analysis.

The changes in LSPR characteristics were analyzed by comparing the optical extinction of copper chalcogenide ternary alloyed nanocrystals with $Cu_{2-x}S$ NCs. Figure 3.3 shows that the LSPR peaks of the copper chalcogenide ternary alloy NCs are blue-shifted, as compared to that of the copper sulfide NCs. A LSPR peak centered at 1355 nm was observed for copper sulfide nanocrystals, while copper selenide-sulfide nanocrystals display a strong near-infrared optical absorption at 990 nm. The copper telluride-sulfide nanocrystals had a broad absorption peak centered at 800 nm, which is blue-shifted more strongly than the other copper chalcogenide NCs. This comparison demonstrates that their LSPR properties can be tuned by controlling the composition of the copper chalcogenide NCs without changing their size.

This blue-shift in the LSPR peak position is likely due to the high concentration of free hole carriers in copper chalcogenide alloy NCs, which arise from the large level of copper vacancies in the material ($Cu_{1.84}S$, $Cu_{1.75}Se_{0.50}S_{0.50}$, and $Cu_{1.65}Te_{0.49}S_{0.51}$, as determined by EDS). There is a

direct relationship between the localized surface plasmon resonance frequency (ω_{sp}) and the bulk plasmon frequency (ω_p), which can be expressed in terms of the square root of the free carrier concentration (N) as follows:[37]

$$\omega_{sp} \propto \omega_p = \sqrt{\frac{Ne^2}{m^* \varepsilon_0}} \tag{3.1}$$

where N is free carrier concentration, e is electron charge, m^* is effective mass, and ε_0 is the permittivity of free space. Thus, higher free carrier concentrations result in an increased LSPR frequency, and a corresponding blue-shift of the peak wavelength. Also, changes in material properties, such as effective hole mass, damping rates, and mobility can lead to a shift of the LSPR peak position.

To support this argument, the free carrier density of the copper chalcogenide nanocrystals was calculated as follows. Using Mie theory, the polarizability (α) of a spherical nanoparticle can be expressed as[13,38]:

$$\alpha = 3\varepsilon_0 V \frac{(\varepsilon - \varepsilon_m)}{(\varepsilon + 2\varepsilon_m)} \tag{3.2}$$

where V is the volume of nanoparticle, ε is the complex dielectric function of the plasmonic nanomaterial and ε_m is the permittivity of the surrounding environment. In Equation 3.2, the denominator should approach zero for a LSPR to occur; that is, when the real part of the permittivity (ε_r) is equal to -2ε_m. According to the Drude model, the real part of the permittivity can be expressed by the frequency of incident light (ω)[14]:

$$\varepsilon_r = 1 - \frac{\omega_p^2}{(\omega^2 + \gamma^2)} \tag{3.3}$$

where ω_p is the bulk plasmon frequency for the material, and γ is the carrier collision frequency. Equation 3.3 can also be expressed in terms of a ratio of energies, where E_p is the bulk plasmon

energy ($E_p = \hbar\omega_p$), E is the energy of the incident radiation ($E = \hbar\omega$), and E_Γ can be interpreted as a damping energy ($E_\Gamma = \hbar\gamma$). By combining the LSPR condition ($\varepsilon_r = -2\varepsilon_m$) in Equation 3.2 with the Drude model, the surface plasmon resonance frequency (ω_{sp}) can be expressed as follows[13]:

$$-2\varepsilon_m = 1 - \frac{\omega_p^2}{(\omega_{sp}^2+\gamma^2)} \tag{3.4}$$

$$\omega_{sp} = \sqrt{\frac{\omega_p^2}{(1+2\varepsilon_m)}} - \gamma^2$$

For the ternary alloyed NCs, the collision frequency (related to the damping energy) can be calculated using the equation by Hsu et al.[38]:

$$E_\Gamma = \mathrm{hc}\frac{\lambda_{FWHM}}{\lambda_{max}^2} \tag{3.5}$$

where h is Planck's constant, c is the speed of light, λ_{FWHM} is the full width at half-maximum (FWHM) of the absorption peak, and λ_{max} is the wavelength of the absorption peak maximum. Prior to the calculation of the free carrier density for the copper chalcogenide NCs, the bulk plasmon frequency of each sample was calculated:

$$\omega_p = \sqrt{\frac{N_h e^2}{\varepsilon_0 m_h}} \tag{3.6}$$

Finally, the free carrier density of each sample was calculated as follows[38]:

$$N_h = \frac{\omega_p^2 \varepsilon_0 m_h}{e^2}$$

where m_h is the hole effective mass. The calculated results are listed in Table 3.2. (See Appendix A for the calculation of the carrier density of each sample.)

Table 3.2. Damping energy, bulk plasmon energy, and carrier density of $Cu_{2-x}S$, $Cu_{2-x}Se_yS_{1-y}$, and $Cu_{2-x}Te_yS_{1-y}$ NCs. The damping energy for the copper sulfide NCs reported below was determined by Caldwell *et al*.[39]

	$Cu_{2-x}S$	**$Cu_{2-x}Se_yS_{1-y}$**	**$Cu_{2-x}Te_yS_{1-y}$**
Damping energy (eV)	0.07 (Ref. 39)	0.54	1.31
Bulk plasmon energy (eV)	2.15	3.20	4.76
Carrier density (cm^{-3})	2.7×10^{21}	3.0×10^{21}	6.4×10^{21}

As shown in Table 3.2, the calculated charge carrier densities of the $Cu_{2-x}S$, $Cu_{2-x}Se_yS_{1-y}$, and $Cu_{2-x}Te_yS_{1-y}$ NCs are 2.7×10^{21}, 3.0×10^{21}, and 6.4×10^{21} cm^{-3}, respectively. As expected from the EDS data, the samples with larger quantities of copper vacancies possess a higher carrier density. This result validates the observed blue shift of the LSPR peak in the copper chalcogenide alloy NCs and corresponds well with other plasmonic studies of the pure $Cu_{2-x}S$, $Cu_{2-x}Se$ and $Cu_{2-x}Te$ NCs.[15] These higher vacancy concentrations could result from the lower electronegativity of selenium and tellurium relative to sulfur, potentially leading to more facile copper vacancy generation. Alternatively, the higher vacancy concentrations could be attributed to increased stress and strain in the alloys caused by the substitution of larger selenium and tellurium atoms for sulfur anions, thus resulting in higher concentrations of vacancies to accommodate lattice relaxation, and leading to a higher charge carrier density.

However, it should be noted that covellite copper sulfide NCs (CuS) have a blue-shifted LSPR peak limited to ~975 nm,[9] despite having very high copper deficiencies. Therefore, the blue shift of the LSPR peak might be also attributed to the significant increase of the bulk

plasmon frequency compared to the increase of the collision frequency (damping energy), which are both material properties determined by each individual alloy.

To gain further insights into the plasmonic properties of each alloy, the molar extinction coefficient was calculated using the absorbance spectrum of copper chalcogenide nanocrystals in toluene with a Cu concentration of 100 ppm (see Appendix A for calculations). Interestingly, it was found that the LSPR peak of the $Cu_{2-x}Te_yS_{1-y}$ NCs exhibited broader and flatter peaks than the other copper selenide-sulfide nanocrystals, even though it has highest free carrier density of the samples that were investigated. Presumably, this weak NIR absorbance is attributed to increased scattering by defects, as larger tellurium anions are substituted for sulfur anions. Thus, an increased collision frequency results in increased damping and a reduced intensity of the LSPR peak.

3.3. Photothermal Conversion Measurements

For practical use in photothermal therapy, the initially hydrophobic copper chalcogenide NCs were made water-dispersible through ligand exchange using mPEG-thiol. The results of the ligand exchange and phase transfer are presented in Figure 3.4. These PEGylated NCs were dispersed well in deionized water without aggregation, as demonstrated by TEM (Figure A.4).

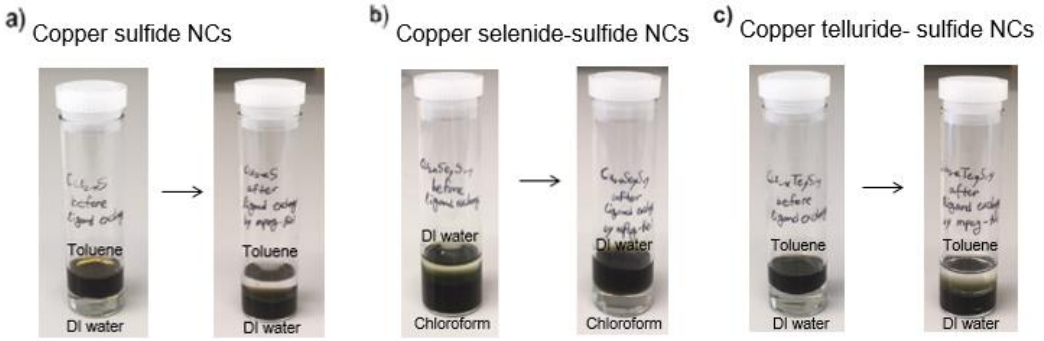

Figure 3.4. Photographs of the (a) $Cu_{2-x}S$, (b) $Cu_{2-x}Se_yS_{1-y}$, and (c) $Cu_{2-x}Te_yS_{1-y}$ NCs dispersed in organic solvents before ligand exchange and in deionized water after ligand exchange.

After successful ligand exchange, the photothermal characteristics of the copper chalcogenide NCs were measured. To measure the photothermal conversion performance of the samples, 3 mL of aqueous PEGylated copper chalcogenide NC dispersions with identical concentrations (100 ppm Cu) were put into quartz cuvettes. Then, the temperature increase of the aqueous dispersions were examined by a thermocouple probe with an accuracy of 0.1°C upon excitation with 2 W of irradiation from a 808 nm laser for 30 min, as shown in Figure 3.5, until the system reached its steady state temperature.

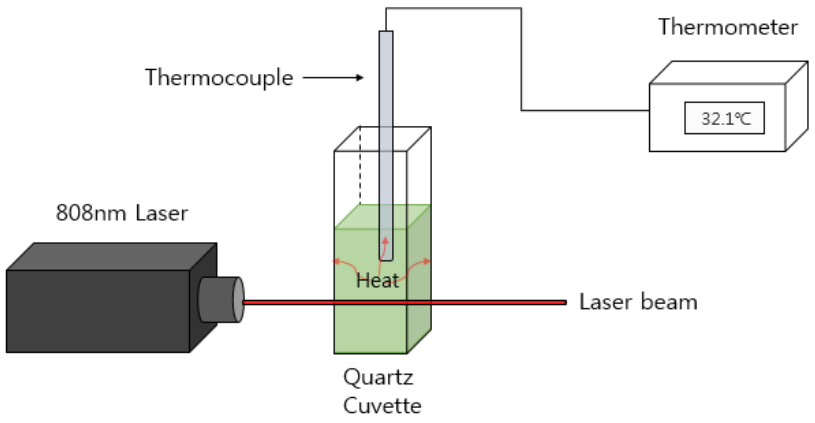

Figure 3.5. Schematic depiction of the photothermal conversion measurement.

Direct laser irradiation of the probe was avoided, and the temperature was recorded every 5 seconds by a digital thermometer. After 30 min, the laser was turned off, and the temperature decrease of the aqueous dispersion was monitored to determine the rate of heat transfer and the photothermal conversion efficiency of the samples.

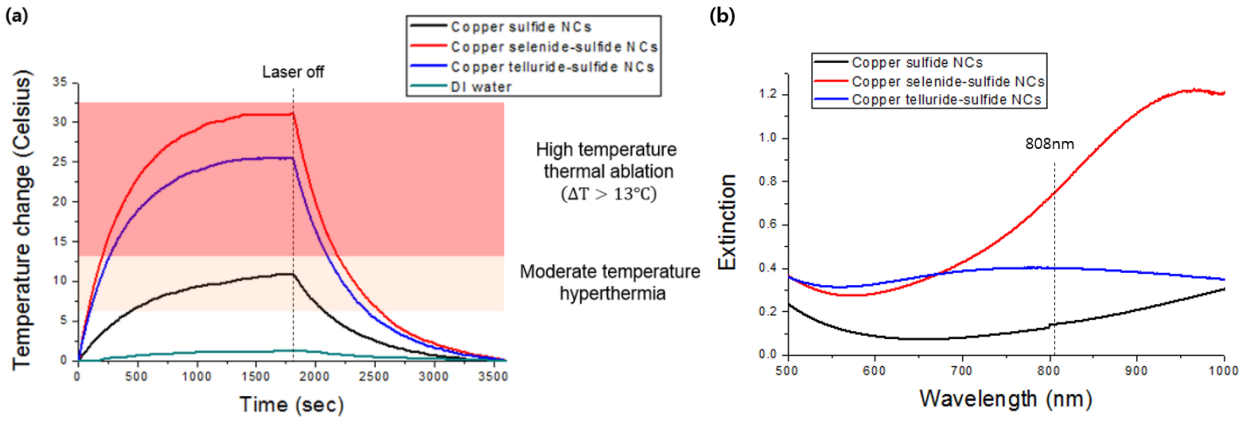

Figure 3.6. (a) Temperature profile of aqueous PEGylated copper chalcogenide NC dispersions with identical copper concentrations (100 ppm) and deionized water. (b) Corresponding extinction spectra.

Figure 3.6 shows the temperature profiles of the aqueous copper chalcogenide nanocrystal dispersions in addition to pure deionized water (*i.e.*, without any photothermal agent), which was used as a control. The temperature of the aqueous PEGylated copper chalcogenide NC dispersions increased rapidly upon laser illumination, and reached steady state in 30 min. After removing the laser source, the temperature returned to ambient conditions by heat dissipation to the surroundings. Under identical conditions, the temperature of deionized water is only increased by 1.3°C relative to room temperature. In contrast, the temperatures of the aqueous dispersions of the copper chalcogenide NCs were increased by 10.9°C, 31.1°C, and 25.5°C in 30 min, corresponding to $Cu_{2-x}S$, $Cu_{2-x}Se_yS_{1-y}$, and $Cu_{2-x}Te_yS_{1-y}$, respectively. This demonstrates that

the copper chalcogenide NCs can efficiently convert the incident 808 nm laser energy into thermal energy.

Importantly, the copper chalcogenide alloy nanocrystals easily reach the high thermal ablation temperatures that effectively kill cancer cells in few minutes (> 4–6 min).[21] In contrast, the temperature increase of the pure copper sulfide nanocrystals was not enough to induce high temperature thermal ablation under the same conditions. The larger temperature increase of the copper chalcogenide alloy nanocrystals can be explained by their large absorption cross section at the laser wavelength (808 nm), which can be inferred from their corresponding extinction spectra. This is due to the fact that nanocrystals having larger absorption cross sections can absorb more incident photons, more effectively converting incident photon energy into thermal energy.

However, this is not a complete description because the absorption cross section of the nanocrystals is not the only factor leading to the observed temperature increase. In combination with the absorption cross section, photothermal conversion efficiency should also be taken into consideration. Therefore, the photothermal conversion efficiency of each sample was studied to evaluate its photothermal conversion performance in depth. The photothermal conversion efficiencies were calculated using an energy balance on the system, as suggested by Roper *et al.*[40] The total energy balance for the system can be expressed as:

$$\sum_i m_i C_{p,i} \frac{dT}{dt} = Q_{in} - Q_{out} \tag{3.7}$$

where m_i and $C_{p,i}$ are the mass and specific heat capacity of component *i* (copper chalcogenide NCs and deionized water, respectively), *T* is the solution temperature, and *t* is the irradiation time. Q_{in} is the heat input from the laser, and Q_{out} is the heat lost to the surrounding environment. In the aqueous copper chalcogenide nanocrystal dispersions, the mass of

nanocrystals (0.0003 g of Cu) is significantly less than that of water (3 g). Hence, Equation 3.7 can be simplified to:

$$m_w C_{p,w} \frac{dT}{dt} = Q_{in} - Q_{out} \tag{3.8}$$

where m_w and $C_{p,w}$ are the mass and specific heat capacity of water, respectively. Since the laser power is fixed, the heat input will be finite. Thus, the accumulation of energy in the system will be zero at steady state where the heat input is equal to the heat output.

$$m_w C_{p,w} \frac{dT}{dt} = Q_{in} - Q_{out} = 0 \tag{3.9}$$

$$Q_{in} = Q_{out}$$

The heat input (Q_{in}) term includes the energy input through light absorption of the copper chalcogenide nanocrystals and light absorption from the experimental cell itself, which was determined to be 21.5 mW (see Appendix A for calculations).

$$Q_{in} = Q_{in,surr} + Q_{in,NCs} \tag{3.10}$$

where $Q_{in,surr}$ is the heat input by the quartz cuvette cell and deionized water, and $Q_{in,NCs}$ is the photothermal energy converted by the nanocrystals under 808 nm laser irradiation, as given by Equation 3.11

$$Q_{in,NCs} = (I_0 - I_{tr})\eta = I_0(1 - 10^{-A_{808}})\eta \tag{3.11}$$

where I_0 is the incident laser power, I_{tr} is the transmitted laser power, η is the photothermal conversion efficiency, and A_{808} is the absorbance of the nanocrystals at a wavelength of 808 nm. Furthermore, the heat output (Q_{out}) term can be expressed through convective heat transfer:

$$Q_{out} = \mathrm{hS(T} - T_{surr}) \tag{3.12}$$

where h is the heat transfer coefficient, S is the surface area of the container, and T_{surr} is the ambient temperature of the surroundings. Finally, the photothermal conversion efficiency (η) of the nanocrystals can be determined by using Equations 3.9, 3.10, 3.11, and 3.12 as follows:

$$Q_{in,surr} + Q_{in,NCs} = Q_{out} \tag{3.13}$$

$$Q_{in,surr} + I_0(1 - 10^{-A_{808}})\eta = \mathrm{hS(T} - T_{surr})$$

By rearranging the above equation, the photothermal conversion efficiency can be expressed as:

$$\eta = \frac{\mathrm{hS(T}-T_{surr})-Q_{in,surr}}{I_0\left(1-10^{-A_{808}}\right)} \tag{3.14}$$

However, the heat transfer coefficient (h) still remains unknown for the calculation of the photothermal conversion efficiency. Thus, the rate of temperature drop after the laser is turned off was used to determine the heat transfer coefficient of each sample. When the laser is turned off, the heat input (Q_{in}) term is zero without the laser irradiation. Therefore, Equation 3.8 becomes:

$$m_w C_{p,w} \frac{dT}{dt} = -Q_{out} = -\mathrm{hS(T} - T_{surr}) \tag{3.15}$$

Rearranging yields Equation 3.16:

$$\frac{dT}{dt} = -\frac{\mathrm{hS(T}-T_{surr})}{m_w C_{p,w}} \tag{3.16}$$

With careful consideration, a dimensionless driving force temperature, θ, is introduced in terms of the maximum temperature achieved by the system, as shown below:

$$\theta = \frac{\mathrm{T}-T_{surr}}{T_{max}-T_{surr}}$$

Differentiating both sides gives

$$\mathrm{d}\theta = \left(\frac{1}{T_{max} - T_{surr}}\right)\mathrm{dT}$$

Thus,

$$\frac{d\theta}{dt} = -\frac{\mathrm{hS}}{m_w C_{p,w}}\theta \tag{3.17}$$

Moreover, rearranging and integrating gives Equation 3.18:

$$-\frac{d\theta}{\theta} = \frac{\mathrm{hS}}{m_w C_{p,w}}\mathrm{dt} \tag{3.18}$$

$$-ln\theta = \frac{\mathrm{hS}}{m_w C_{p,w}}\mathrm{t}$$

In addition, a characteristic time constant, $\tau_s = \frac{m_w C_{p,w}}{hs}$, is defined for convenience. Characteristic time constants for heat transfer from the system were determined by plotting cooling time on a linear scale versus the negative natural logarithm of the driving force temperature, as shown in Figure 3.7.

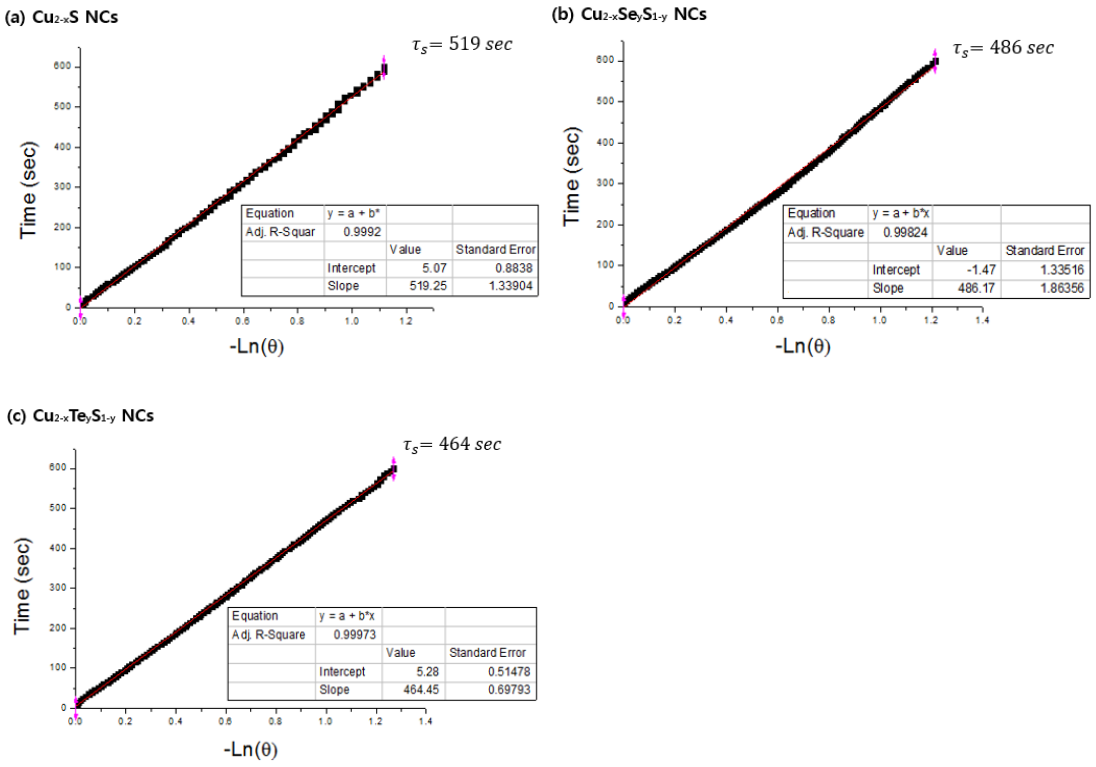

Figure 3.7. Characteristic time constants for (a) $Cu_{2-x}S$, (b) $Cu_{2-x}Se_yS_{1-y}$, and (c) $Cu_{2-x}Te_yS_{1-y}$ NCs dispersed in deionized water.

As can be seen from Figure 3.7, the characteristic time constant of each sample was found, and the heat transfer coefficient was evaluated based on the characteristic time constant for the calculation of photothermal conversion efficiency. According to the above formulas for the determination of the heat transfer coefficient and photothermal conversion efficiency, the photothermal conversion efficiencies of the various copper chalcogenide NCs were calculated, and are tabulated with their LSPR peak wavelength in Table 3.3.

Table 3.3. The calculated photothermal conversion efficiencies of the $Cu_{2-x}S$, $Cu_{2-x}Se_yS_{1-y}$, and $Cu_{2-x}Te_yS_{1-y}$ NCs and their LSPR peak wavelengths.

	$Cu_{2-x}S$	$Cu_{2-x}Se_{1-y}S_y$	$Cu_{2-x}Te_{1-y}S_y$
Photothermal conversion efficiency (η)	45.6%	49.4%	56.8%
LSPR peak wavelength	1355 nm	990 nm	800 nm

Table 3.3 shows the calculated photothermal conversion efficiencies of the $Cu_{2-x}S$, $Cu_{2-x}Se_yS_{1-y}$, and $Cu_{2-x}Te_yS_{1-y}$ NCs: 45.6%, 49.4%, and 56.8%, respectively. Overall, the calculated photothermal conversion efficiencies of the copper chalcogenide NCs reveal that they efficiently convert photon energy into heat energy with 808 nm laser irradiation, which is widely used for photothermal therapy due to its position within the NIR tissue transparency window. Among the copper chalcogenide nanocrystals investigated, $Cu_{2-x}Te_yS_{1-y}$ NCs (56.8%) possess the highest photothermal conversion efficiency. Moreover, as can be seen in Table 3.3 the photothermal conversion efficiency increases significantly as the LSPRs peak wavelength becomes closer to the incident excitation wavelength (808 nm), which is in agreement with

several other studies.[2,8] These results give insights into the potential of the as-of-yet unexplored use of copper telluride-sulfide and copper selenide-sulfide NCs in photothermal therapy.

Chapter 4. CONCLUSIONS

In summary, the LSPR properties of copper chalcogenide alloy NCs and their potential use for photothermal therapy were investigated through a comparison study with copper sulfide NCs. Comparison of the extinction spectra of $Cu_{2-x}S$ (~5.2nm), $Cu_{2-x}Se_yS_{1-y}$ (~6.5nm), and $Cu_{2-x}Te_yS_{1-y}$ (~6.2nm) clearly shows that their LSPR properties can be actively tuned by controlling elemental composition. The LSPR peak positions of the copper chalcogenide alloy NCs are blue-shifted as larger chalcogen atoms (Se and Te) are substituted into the sulfur sublattice. We believe that this mainly occurs due to the stabilization of higher concentrations of free holes, but also as a function of changes in material properties, such as effective hole mass, damping rates, and mobility.

Furthermore, the alloys have an increased absorption intensity in the NIR window (650 – 900 nm) with identical copper concentrations, as compared to pure copper sulfide NCs. Due to their strong absorption in the NIR window, $Cu_{2-x}Se_yS_{1-y}$, and $Cu_{2-x}Te_yS_{1-y}$ NCs at a Cu concentration of 100 ppm can increase the temperature of the aqueous dispersion by 31.1°C, and 25.5°C, respectively, in 30 min under 2 W of incident 808 nm laser irradiation. In contrast, the temperature of the aqueous dispersion of pure copper sulfide NCs is increased by 10.9°C under the same conditions.

The calculated photothermal conversion efficiency of the nanocrystals shows that the $Cu_{2-x}Se_yS_{1-y}$, and $Cu_{2-x}Te_yS_{1-y}$ NCs possess higher efficiencies than that of $Cu_{2-x}S$ NCs, as their

LSPR peaks are more closely matched to the laser wavelength. The photothermal conversion efficiency of the $Cu_{2-x}Te_yS_{1-y}$ NCs was calculated to be 56.8%, which is higher than that of the $Cu_{2-x}Se_yS_{1-y}$ (49.4%) and $Cu_{2-x}S$ NCs (45.6%). Such a combination of high photothermal conversion efficiency and large absorption cross section enables the alloy NCs to raise the local temperature more effectively than that of $Cu_{2-x}S$ NCs with 808 nm laser irradiation.

Since photothermal agents with high photothermal conversion capabilities can increase local temperature more effectively, they can potentially kill cancer cells with shorter irradiation time, or a lower laser power density. Therefore, it is expected that copper selenide-sulfide and copper telluride-sulfide NCs could be quite promising as photothermal agents for near-infrared laser induced photothermal therapy.

Chapter 5. FUTURE DIRECTIONS

For these materials to be implemented practically as photothermal agents, future work must be directed towards evaluating the cytotoxicity of copper chalcogenide alloy nanocrystals. Low cytotoxicity must be ensured in order to prevent damage to healthy cells. Although alloy NCs increase the photothermal conversion efficiency and normalized temperature increase, as compared to pure copper sulfide NCs, the addition of tellurium and selenium has the potential to increase cytotoxicity.[41] Therefore, in addition to evaluating cytotoxicity, additional efforts should be directed towards actively decreasing the toxicity of the nanocrystals. One such strategy would be to intrinsically decrease the toxicity of the nanomaterial by incorporating non-toxic elements in place of selenium and tellurium. For example, copper bismuth sulfide (Cu_3BiS_3) nanocrystals

are potential photothermal candidates that may have lower cytotoxicity, since bismuth is exceptionally nontoxic to the human body, even in high doses.[42]

In addition, it is possible to decrease the toxicity of chemically identical materials significantly by altering several physicochemical properties, such as surface chemistry, shape, absorption gradient and surface smoothness or roughness.[41] From this viewpoint, the encapsulation of nanocrystals with silica shells, or other biologically-inert coatings – such as those implemented in widely-used systems like CdSe-ZnS core-shell quantum dots[43] – could be a viable strategy to decrease the toxicity of these promising nanomaterials.

REFERENCES

(1) Zhou, M.; Tian, M.; Li, C. *Bioconjug. Chem.* **2016**, *27*, 1188-1199.

(2) Li, B.; Wang, Q.; Zou, R.; Liu, X.; Xu, K.; Li, W.; Hu, J. *Nanoscale* **2014**, *6* (6), 3274–3282.

(3) Wang, S. H.; Riedinger, A.; Li, H. B.; Fu, C. H.; Liu, H. Y.; Li, L. L.; Liu, T. L.; Tan, L. F.; Barthel, M. J.; Pugliese, G.; De Donato, F.; D'Abbusco, M. S.; Meng, X. W.; Manna, L.; Meng, H.; Pellegrino, T. *ACS Nano* **2015**, *9* (2), 1788–1800.

(4) Goel, S.; Chen, F.; Cai, W. *Small* **2014**, *10* (4), 631–645.

(5) Hessel, C. M.; P. Pattani, V.; Rasch, M.; Panthani, M. G.; Koo, B.; Tunnell, J. W.; Korgel, B. A. *Nano Lett.* **2011**, *11* (6), 2560–2566.

(6) Li, W.; Zamani, R.; Gil, P. R.; Pelaz, B.; Ibáñez, M.; Cadavid, D.; Shavel, A.; Alvarez-puebla, R. A.; Parak, W. J.; Arbiol, J.; Cabot, A.; Pelaz, Ψ. B.; Ibáñez, Ψ. M. *J. Am. Chem. Soc.* **2013**, *135*, 7098–7101.

(7) Saldanha, P. L.; Brescia, R.; Prato, M.; Li, H.; Povia, M.; Manna, L.; Lesnyak, V. *Chem. Mater.* **2014**, *26* (3), 1442–1449.

(8) Chen, H.; Shao, L.; Ming, T.; Sun, Z.; Zhao, C.; Yang, B.; Wang, J. *Small* **2010**, *6* (20), 2272–2280.

(9) Comin, A.; Manna, L. *Chem. Soc. Rev.* **2014**, *43* (11), 3957–3975.

(10) Willets, K. A.; Duyne, R. Van; Van Duyne, R. P. *Annu. Rev. Phys. Chem.* **2007**, *58* (1), 267–297.

(11) Anker, J. N.; Hall, W. P.; Lyandres, O.; Shah, N. C.; Zhao, J.; Van Duyne, R. P. *Nat. Mater.* **2008**, *7* (6), 442–453.

(12) Liu, X.; Swihart, M. T. *Chem. Soc. Rev.* **2014**, *43* (11), 3908–3920.

(13) Luther, J. M.; Jain, P. K.; Ewers, T.; Alivisatos, a P. *Nat. Mater.* **2011**, *10* (5), 361–366.

(14) Dorfs, D.; Hartling, T.; Miszta, K.; Bigall, N. C.; Kim, M. R.; Genovese, A.; Falqui, A.; Povia, M.; Manna, L. *J. Am. Chem. Soc.* **2011**, *133* (29), 11175–11180.

(15) Kriegel, I.; Jiang, C.; Rodriguez-Fernandez, J.; Schaller, R. D.; Talapin, D. V.; Da Como, E.; Feldmann, J. *J. Am. Chem. Soc.* **2012**, *134* (3), 1583–1590.

(16) Kanehara, M.; Koike, H.; Yoshinaga, T.; Teranishi, T. *J. Am. Chem. Soc.* **2009**, *131* (49), 17736–17737.

(17) Buonsanti, R.; Llordes, A.; Aloni, S.; Helms, B. A.; Milliron, D. J. *Nano Lett.* **2011**, *11* (11), 4706–4710.

(18) Rowe, D. J.; Jeong, J. S.; Mkhoyan, K. A.; Kortshagen, U. R. *Nano Lett.* **2013**, *13*, 1317-1322.

(19) Faucheaux, J. a.; Stanton, A. L. D.; Jain, P. K. *J. Phys. Chem. Lett.* **2014**, *5* (6), 976–985.

(20) Huang, X.; El-sayed, M. A. *Alexandria J. Med.* **2011**, *47* (1), 1–9.

(21) Stauffer, P. R.; Goldberg, S. N. *Int. J. Hyperthermia* **2004**, *20* (7), 671–677.

(22). Dickerson, E. B.; Dreaden, E. C.; Huang, X.; El-Sayed, I. H.; Chu, H.; Pushpanketh, S.; McDonald, J. F.; El-Sayed, M. A. *Cancer Lett.* **2008**, *269* (1), 57–66.

(23) Zhou, J.; Lu, Z.; Zhu, X.; Wang, X.; Liao, Y.; Ma, Z.; Li, F. *Biomaterials* **2013**, *34* (37), 9584–9592.

(24) Zhou, S.-M.; Ma, D.-K.; Zhang, S.-H.; Wang, W.; Chen, W.; Huang, S.-M.; Yu, K. *Nanoscale* **2016**, *8* (3), 1374–1382.

(25) Weissleder, R. *Nature biotech.*. **2001**, *19*, 316–317.

(26) Wang, Y.; Black, K. C. L.; Luehmann, H.; Li, W.; Zhang, Y.; Cai, X.; Wan, D.; Al, W. E. T. **2013**, 2068–2077.

(27) Huang, X.; El-Sayed, I. H.; Qian, W.; El-Sayed, M. A. *J. Am. Chem. Soc.* **2006**, *128* (6), 2115–2120.

(28) Chen, J.; Wang, D.; Xi, J.; Au, L.; Siekkinen, A.; Warsen, A.; Li, Z. Y.; Zhang, H.; Xia, Y.; Li, X. *Nano Lett.* **2007**, *7* (5), 1318–1322.

(29) Zha, Z.; Yue, X.; Ren, Q.; Dai, Z. *Adv. Mater.* **2013**, *25* (5), 777–782.

(30) Liu, X.; Li, B.; Fu, F.; Xu, K.; Zou, R.; Wang, Q.; Zhang, B.; Chen, Z.; Hu, J. *Dalton Trans.* **2014**, *43* (30), 11709–11715.

(31) Huang, Y.; Lai, Y.; Shi, S.; Hao, S.; Wei, J.; Chen, X. *Chem. - An Asian J.* **2015**, *10* (2), 370–376.

(32) Liu, X.; Wang, X.; Swihart, M. T. *Chem. Mater.* **2013**, 25, 4402-4408.

(33) Chen, O.; Zhao, J.; Chauhan, V. P.; Cui, J.; Wong, C.; Harris, D. K.; Wei, H.; Han, H.-S.; Fukumura, D.; Jain, R. K.; Bawendi, M. G. *Nat. Mater.* **2013**, *12* (5), 445–451.

(34) Jiang, K.; Smith, D. A.; Pinchuk, A. *J. Phys. Chem. C* **2013**, *117* (51), 27073–27080.

(35) Jain, P. K.; Manthiram, K.; Engel, J. H.; White, S. L.; Faucheaux, J. A.; Alivisatos, A. P. *Angew. Chemie - Int. Ed.* **2013**, *52* (51), 13671–13675.

(36) Zhao, Y.; Pan, H.; Lou, Y.; Qiu, X.; Zhu, J.; Burda, C. *J. Am. Chem. Soc.* **2009**, *131* (12), 4253–4261.

(37) Garcia, G.; Buonsanti, R.; Runnerstrom, E. L.; Mendelsberg, R. J.; Llordes, A.; Anders, A.; Richardson, T. J.; Milliron, D. J. *Nano Lett.* **2011**, *11* (10), 4415–4420.

(38) Hsu, S.-W.; On, K.; Tao, A. R. *J. Am. Chem. Soc.* **2011**, *133* (47), 19072–19075.

(39) Caldwell, A. H.; Ha, D.-H.; Ding, X.; Robinson, R. D. *J. Chem. Phys.* **2014**, *141* (16), 164125.

(40) Roper, D. K.; Ahn, W.; Hoepfner, M. *J. Phys. Chem. C* **2007**, *111* (9), 3636–3641.

(41) van der Merwe, D.; Pickrell, J. A. *Vet. Toxicol.* **2012**, 383–390.

(42) Rodilla, V.; Miles, A. T.; Jenner, W.; Hawksworth, G. M. *Chem. Biol. Interact.* **1998**, *115* (1), 71–83.

(43) Kirchner, C.; Liedl, T.; Kudera, S.; Pellegrino, T.; Javier, A. M.; Gaub, H. E.; Stölzle, S.; Fertig, N.; Parak, W. J. *Nano Lett.* **2005**, *5* (2), 331–338.

(44) Cai, X.; Jia, X.; Gao, W.; Zhang, K.; Ma, M.; Wang, S.; Zheng, Y.; Shi, J.; Chen, H. *Adv. Funct. Mater.* **2015**, *25* (17), 2520–2529.

(45) O. Madelung; U. Rössler; M. Schulz. *Non-Tetrahedrally Bonded Elements and Binary Compounds I*, **1998**, *41c*,1-9

APPENDIX A

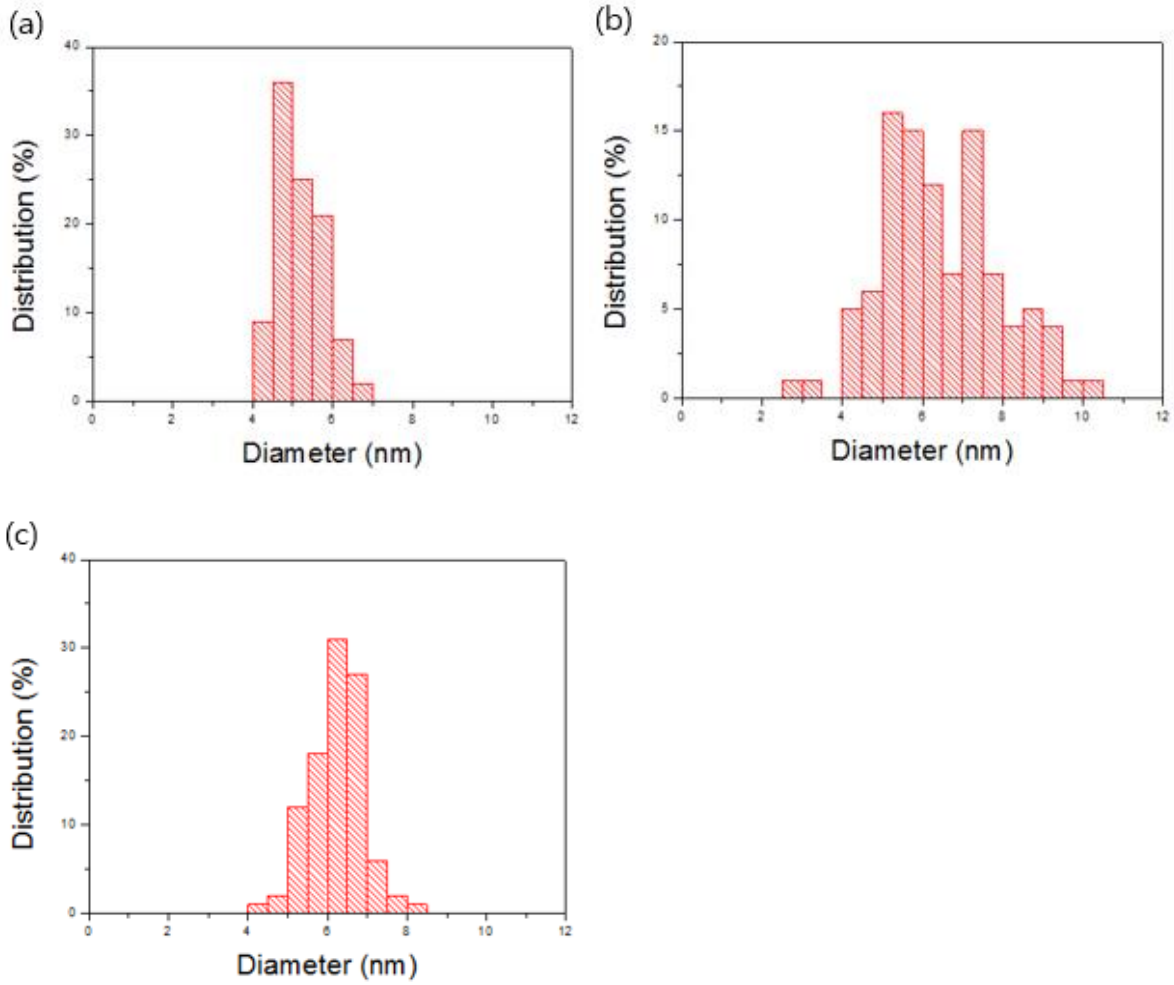

Figure A.1. Size distribution of the (a) $Cu_{2-x}S$, (b) $Cu_{2-x}Se_yS_{1-y}$, and (c) $Cu_{2-x}Te_yS_{1-y}$ NCs shown in Figure 3.1.

(a) $Cu_{2-x}S$ NCs

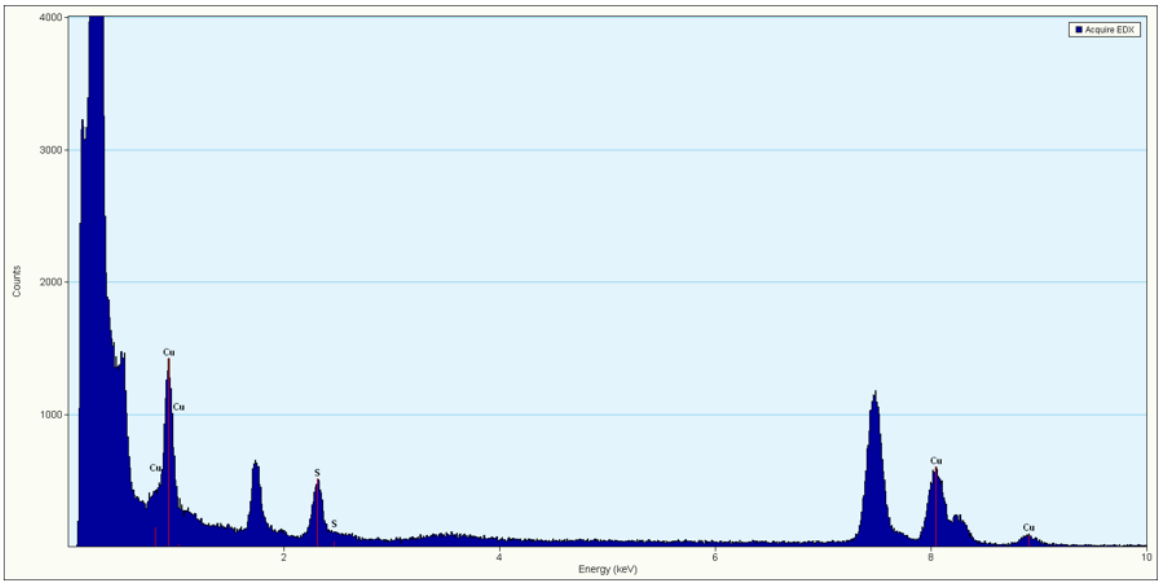

(b) $Cu_{2-x}Se_ySe_{1-y}$ NCs

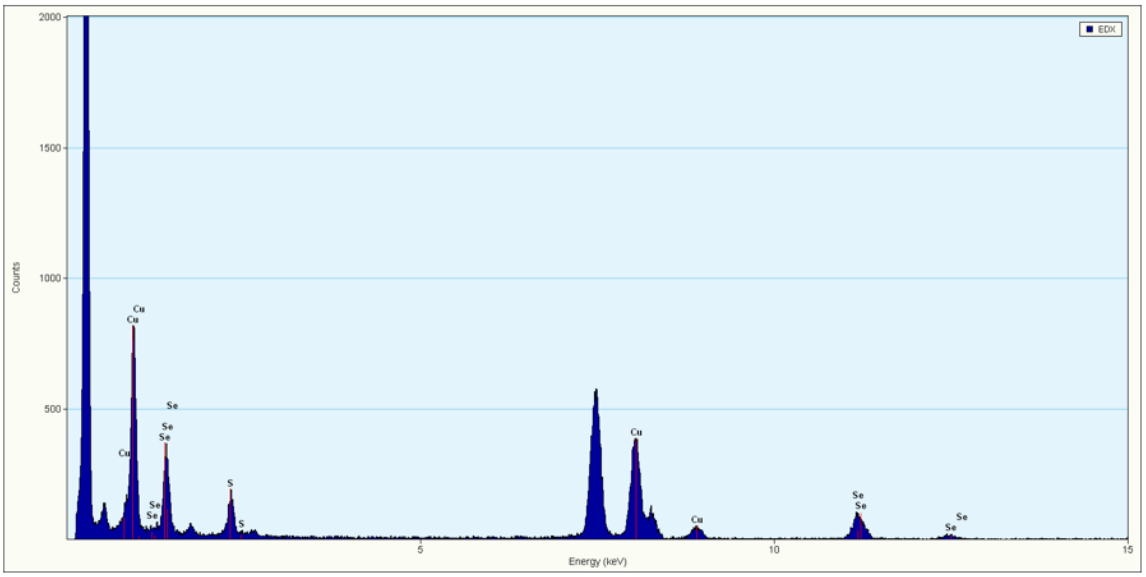

(c) $Cu_{2-x}Te_yS_{1-y}$ NCs

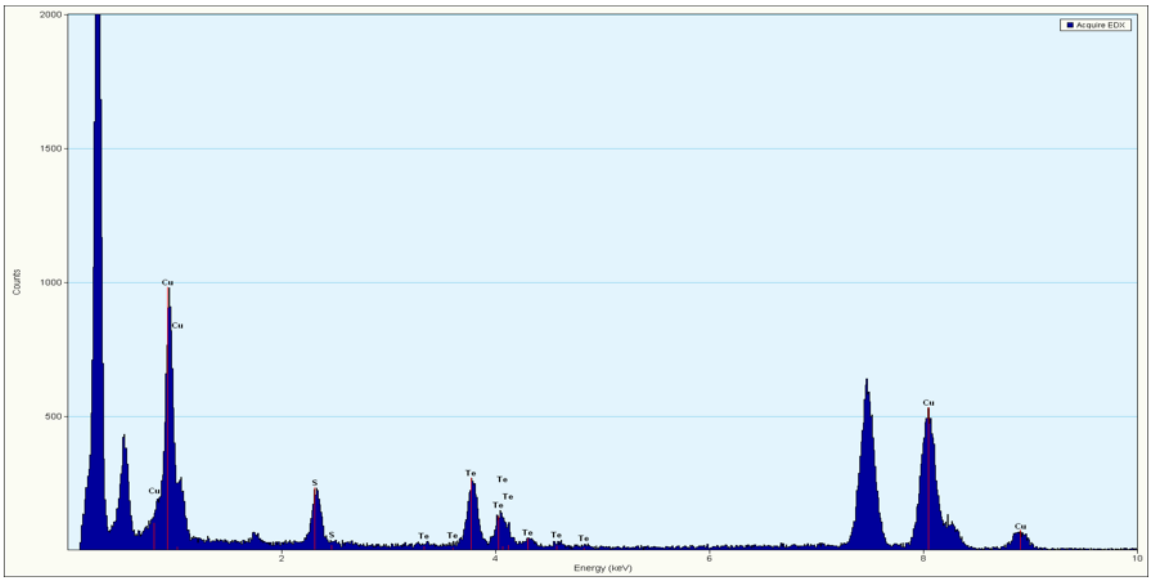

Figure A.2. EDS spectra of (a) $Cu_{2-x}S$, (b) $Cu_{2-x}Se_yS_{1-y}$, and (c) $Cu_{2-x}Te_yS_{1-y}$ NCs.

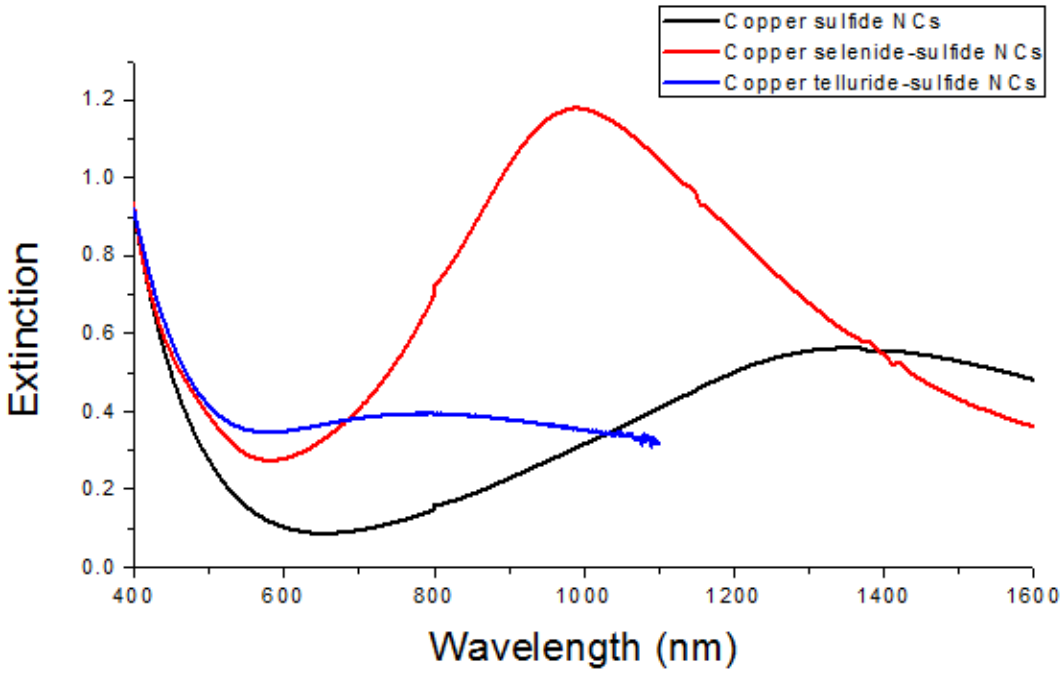

Figure A.3. Extinction spectra of (a) $Cu_{2-x}S$, (b) $Cu_{2-x}Se_yS_{1-y}$, and (c) $Cu_{2-x}Te_yS_{1-y}$ NCs dispersed in toluene with Cu concentrations of 100 ppm.

The molar extinction coefficient of the copper chalcogenide NCs was calculated according to the Beer-Lambert law,

$$A = \varepsilon LC \tag{A.1}$$

where A is the absorbance, ε is the molar extinction coefficient ($M^{-1}cm^{-1}$), L is the path length (1 cm), and C is the molar concentration (mol/L). The molar concentration of the nanocrystals can be calculated as follows[44]:

$$\varepsilon = \frac{A}{LC} = \frac{AV\rho_{NC}N_A}{LC_{wt,NC}} \tag{A.2}$$

where V is the volume of nanocrystals (cm^3), ρ_{NC} is the density of the nanocrystals (g/cm^3), N_A is Avogadro's constant, and C_{wt} is the mass concentration of nanocrystals (g/L). The values used in the calculation of the extinction coefficient are listed in Table A.1.

Table A.1. Values used in the calculation of the extinction coefficient for each sample.

	Radius (nm)	**Density (g/cm3)**	**Mass concentration (g/L)**
$Cu_{2-x}S$	2.6	5.6	0.1274
$Cu_{2-x}Se_yS_{1-y}$	3.25	6.67*	0.1501
$Cu_{2-x}Te_yS_{1-y}$	3.1	7.11*	0.1766

*Densities of copper chalcogenide alloy nanocrystals were calculated on the basis of the EDS compositional data.

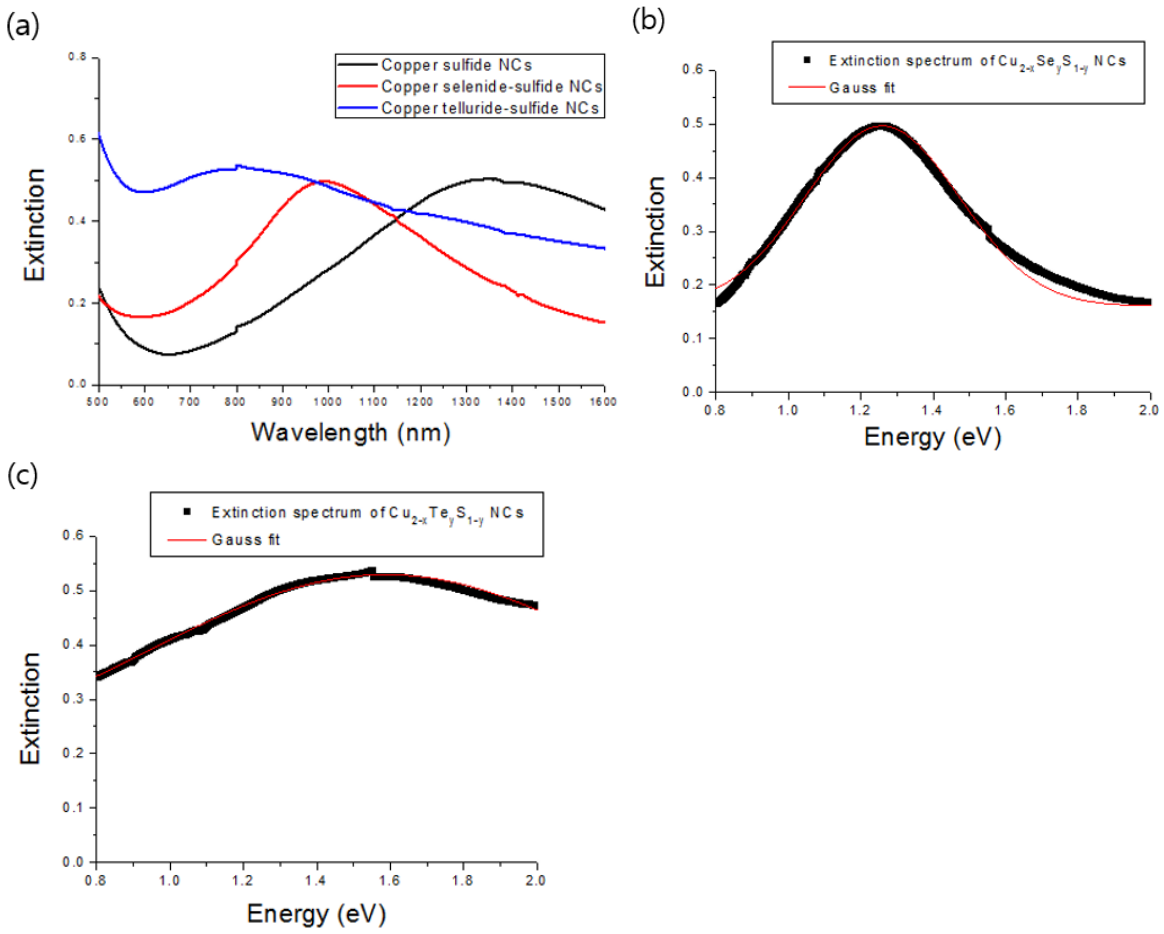

Figure A.4. (a) Extinction spectra of $Cu_{2-x}S$, $Cu_{2-x}Se_yS_{1-y}$, and $Cu_{2-x}Te_yS_{1-y}$ NCs dispersed in toluene. The corresponding full width at half-maximum (FWHM) of the extinction spectra of (b) $Cu_{2-x}Se_yS_{1-y}$, and (c) $Cu_{2-x}Te_yS_{1-y}$ NCs.

The charge carrier density of copper chalcogenide NCs was calculated based on their bulk plasmon frequency (ω_p), which can be expressed by the equation A.3.

$$\omega_p = \sqrt{\frac{N_h e^2}{\varepsilon_0 m_h}} \tag{A.3}$$

Prior to the calculation of the charge carrier density, the bulk plasmon frequency of the copper chalcogenide NCs was calculated using the relationship between the LSPR frequency (ω_{sp}) and the bulk plasmon oscillation frequency (ω_p), as expressed by Equation A.4

$$\omega_{sp} = \sqrt{\frac{\omega_p^2}{(1+2\varepsilon_m)} - \gamma^2} \tag{A.4}$$

Table A.2. Values for calculation of the bulk plasmon frequency of the samples.

	λ_{FWHM} (nm)	λ_{max} (nm)	E_{sp} (eV)	ω_{sp} (sec^{-1})	E_Γ (eV)	γ (sec^{-1})	ε_m
$Cu_{2-x}S$	-	1355	0.91	1.4×10^{15}	-	1×10^{14}(Ref.39)	2.25
$Cu_{2-x}Se_yS_{1-y}$	426	990	1.25	1.9×10^{15}	0.54	8×10^{14}	2.25
$Cu_{2-x}Te_yS_{1-y}$	676	800	1.55	2.4×10^{15}	1.31	2×10^{15}	2.25

Using the data from Figure A.4 and Reference 39, the bulk plasmon frequencies of the copper chalcogenide NCs were calculated as follows:

(a) $Cu_{2-x}S$ NCs

$$\omega_p = \sqrt{(1+2\varepsilon_m)\left(\omega_{sp}^2 + \gamma^2\right)} = \sqrt{(1+2*2.25)((1.4\times10^{15})^2 + (1\times10^{14})^2)}$$

$$= 3.27 \times 10^{15} sec^{-1}$$

(b) $Cu_{2-x}Se_yS_{1-y}$ NCs

$$\omega_p = \sqrt{(1+2\varepsilon_m)\left(\omega_{sp}^2 + \gamma^2\right)} = \sqrt{(1+2*2.25)((1.9\times10^{15})^2 + (8\times10^{14})^2)}$$

$$= 4.86 \times 10^{15} sec^{-1}$$

(c) $Cu_{2-x}Te_yS_{1-y}$ NCs

$$\omega_p = \sqrt{(1+2\varepsilon_m)\left(\omega_{sp}^2 + \gamma^2\right)} = \sqrt{(1+2*2.25)((2.4\times10^{15})^2 + (2\times10^{15})^2)}$$

$$= 7.23 \times 10^{15} sec^{-1}$$

Table A.3. Values for calculation of the free carrier density of the samples.

	ω_p (sec^{-1})	ε_0 ($A^2 \cdot sec^4 \cdot kg^{-1} \cdot m^{-3}$)	e ($A \cdot sec$)	m_h (kg)
$Cu_{2-x}S$	3.27×10^{15}	8.854×10^{-12}	1.602×10^{-19}	$0.8m_0$
$Cu_{2-x}Se_yS_{1-y}$	4.86×10^{15}	8.854×10^{-12}	1.602×10^{-19}	$0.4m_0$
$Cu_{2-x}Te_yS_{1-y}$	7.23×10^{15}	8.854×10^{-12}	1.602×10^{-19}	$0.39m_0$

The effective hole masses of $Cu_{2-x}S$, $Cu_{2-x}Se_yS_{1-y}$, and $Cu_{2-x}Te_yS_{1-y}$ were determined from Reference 39, 13, and 45, respectively, where m_0 is the electron mass (9.1×10^{-31}kg).

According to Equation A.3, the hole carrier density of the copper chalcogenide NCs was calculated as follows:

$$N_h = \frac{{\omega_p}^2 \varepsilon_0 m_h}{e^2} \tag{A.5}$$

(a) $Cu_{2-x}S$ NCs

$$N_h = \frac{(3.27 \times 10^{15} s^{-1})^2 \cdot \left(8.854 \times 10^{-12} \frac{A^2 \cdot s^4}{kg^{-1} \cdot m^{-3}}\right) \cdot 0.8(9.1 \times 10^{-31} kg)}{(1.602 \times 10^{-19} A \cdot s)^2}$$

$$= 2.69 \times 10^{27} m^{-3} = 2.69 \times 10^{21} cm^{-3}$$

(b) $Cu_{2-x}Se_yS_{1-y}$ NCs

$$N_h = \frac{(4.86 \times 10^{15} s^{-1})^2 \cdot \left(8.854 \times 10^{-12} \frac{A^2 \cdot s^4}{kg^{-1} \cdot m^{-3}}\right) \cdot 0.4(9.1 \times 10^{-31} kg)}{(1.602 \times 10^{-19} A \cdot s)^2}$$

$$= 2.97 \times 10^{27} m^{-3} = 2.97 \times 10^{21} cm^{-3}$$

(c) $Cu_{2-x}Te_yS_{1-y}$ NCs

$$N_h = \frac{(7.23 \times 10^{15} s^{-1})^2 \cdot \left(8.854 \times 10^{-12} \frac{A^2 \cdot s^4}{kg^{-1} \cdot m^{-3}}\right) \cdot 0.39(9.1 \times 10^{-31} kg)}{(1.602 \times 10^{-19} A \cdot s)^2}$$

$$= 6.40 \times 10^{27} m^{-3} = 6.40 \times 10^{21} cm^{-3}$$

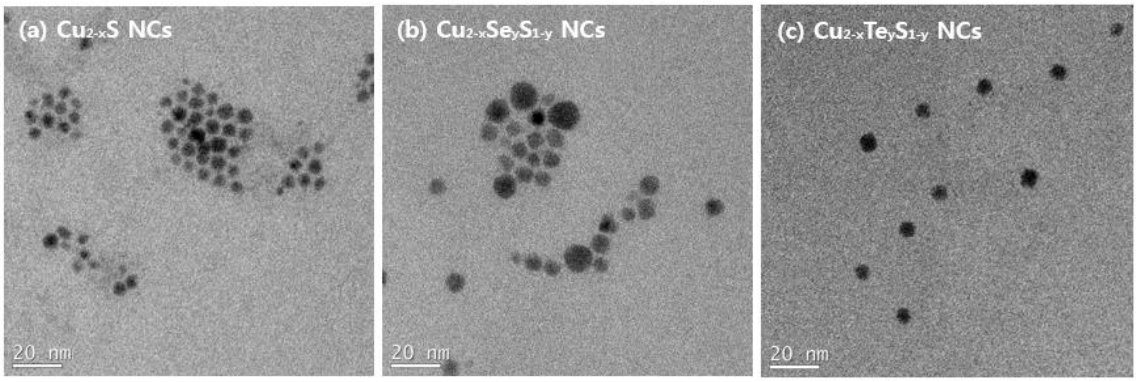

Figure A.5. TEM images of (a) $Cu_{2-x}S$, (b) $Cu_{2-x}Se_yS_{1-y}$, and (c) $Cu_{2-x}Te_yS_{1-y}$ NCs after ligand exchange.

The images shown in Figure A.4 demonstrate successful ligand exchange with limited nanocrystal aggregation.

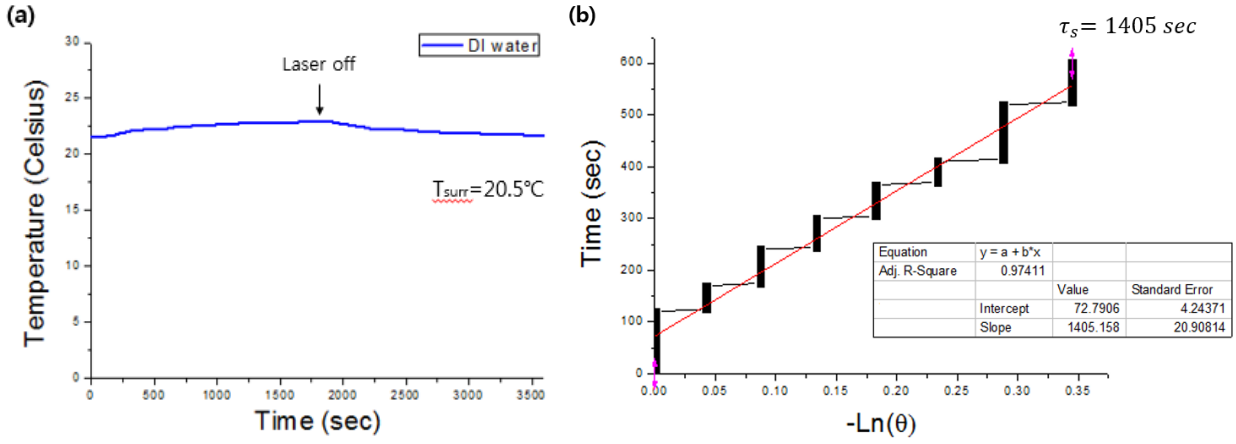

Figure A.6. Temperature profile and characteristic time constant of pure deionized water.

The heat input to the system ($Q_{in,surr}$) by the quartz cuvette cell and deionized water was calculated by using the relationship between the heat input and the heat lost to the surrounding environment at steady state:

$$m_w C_{p,w} \frac{dT}{dt} = Q_{in,surr} - Q_{out} = 0 \tag{A.6}$$

$$Q_{in,surr} = Q_{out}$$

Moreover, the characteristic time constant of the pure deionized water was used to calculate the heat output term as follows:

$$Q_{out} = \mathrm{hS}(T_{Max} - T_{surr}) = \frac{m_w C_{p,w}}{\tau_s}(T_{Max} - T_{surr}) \quad \text{(A.7)}$$

$$= \frac{(3g)\left(\frac{4.2J}{g} \cdot {}^{\circ}C\right)}{1405s}(22.9°C - 20.5°C)$$

$$= 21.5\ mW$$

Therefore, the heat input from the surroundings upon laser irradiation for 30 min is:

$$Q_{in,surr} = Q_{out} = 21.5mW$$